GFZ
Helmholtz-Zentrum
POTSDAM

Originally published as:

Dzieran, L., Thorwart, M., Rabbel, W., Ritter, O. (2019): Quantifying interface responses with seismoelectric spectral ratios. - *Geophysical Journal International*, *217*, 1, pp. 108—121.

DOI: http://doi.org/10.1093/gji/ggz010

Geophysical Journal International

Geophys. J. Int. (2019) **217,** 108–121
Advance Access publication 2019 January 10
GJI Seismology

doi: 10.1093/gji/ggz010

Quantifying interface responses with seismoelectric spectral ratios

L. Dzieran [1], M. Thorwart,[1] W. Rabbel[1] and O. Ritter[2]

[1]*Institute of Geosciences, Christian-Albrechts-University Kiel, 24118 Kiel, Germany. E-mail: laura.dzieran@ifg.uni-kiel.de*
[2]*GFZ German Research Centre for Geosciences, 14473 Potsdam, Germany*

Accepted 2019 January 5. Received 2018 December 30; in original form 2018 August 28

SUMMARY

We investigate seismoelectric (SE) signals accompanying seismic waves radiated from earthquake sources. SE signals are mostly generated from compressional portions of seismic waves by electrokinetic coupling. They contain coseismic electric fields travelling with seismic wave velocity and interface response (IR) waves, which originate at layer interfaces and travel with electromagnetic wave speed. IR wave amplitudes are sensitive to contrasts in poroelastic and electric rock parameters. We introduce SE spectral ratios (SESRs) as a tool to evaluate the influence of IRs on the overall SE signal independently of the earthquake source–time function. Based on data from Northern Chile we show that SESRs show a site specific frequency dependence with a trend of decreasing amplitudes towards increasing frequency. Modelling results reveal that the specific frequency dependence of the SESRs is caused by IRs excited at depths of some hundred metres underneath the recording stations. We analyse the SESR sensitivity towards porosity, permeability, fluid salinity and the depth of the interfaces. We verify that observed SESRs can be reproduced through forward modelling and linearized inversion based on realistic subsurface parameters.

Key words: Electrical properties; Permeability and porosity; Numerical modelling; Wave propagation; Interface waves.

1 INTRODUCTION

On multiple occasions a great resemblance has been observed between seismograms and electric signals of earthquakes (e.g. Honkura *et al.* 2000; Nagao *et al.* 2000; Matsushima *et al.* 2002; Huang 2011; Gao *et al.* 2016; Dzieran *et al.* 2019). A variety of explanations for this phenomenon exist, such as piezoelectric origins (Huang 2002) or a seismic dynamo effect, suggesting that the electric signals are induced by a conductive crust vibrating in the Earth's magnetic field (e.g. Honkura *et al.* 2000; Matsushima *et al.* 2013; Gao *et al.* 2014). At present, the most widely accepted explanation is electrokinetic coupling caused by fluid movement relatively to pore surfaces (e.g. Gao & Hu 2010; Gershenzon *et al.* 2014; Ren *et al.* 2014; Gao *et al.* 2016).

The theory of electrokinetic coupling has been investigated sporadically since the mid of the last century (e.g. Ivanov 1939; Frenkel 1944; Thompson & Gist 1993). An essential step forward in the quantitative understanding of this effect was made by Pride (1994), who developed a set of macroscopic equations for the coupling between the seismic and electromagnetic (EM) waves in a fully saturated medium based on Biot's theory (Biot 1956, 1962) and Maxwell's equations. Pride's theory provided the basis for further investigations on the electrokinetic effect (e.g. Haartsen & Pride 1997; Jardani *et al.* 2010; Ren *et al.* 2010; Schakel *et al.* 2011; Grobbe & Slob 2016). Garambois & Dietrich (2001) used Pride's theory to derive transfer functions between the seismic and electric field in the seismic frequency range. Warden *et al.* (2013) extended Pride's formulae to partially saturated media. An alternative approach for partially saturated media was developed by Revil & Mahardika (2013) and Jardani & Revil (2015). In 2016, Jouniaux & Zyserman published a review on electrokinetically induced seismoelectric (SE), electroseismic and seismomagnetic signals for Earth sciences.

During the passage of seismic waves the electrokinetic effect creates two types of EM waves forming the so-called SE field: coseismic waves and interface responses (IRs).

The electric coseismic wave is an electric signal coupled to the seismic wavefield, travelling with the same velocity. According to Garambois & Dietrich (2001), the electric field amplitudes of these waves are directly proportional to ground acceleration connected with compressional movement. Numerical studies showed that *SH* waves are also accompanied by coseismic electric signals, however their amplitudes are expected to be much smaller than those caused by *P* waves (Bordes *et al.* 2015; Zyserman *et al.* 2016). Therefore, it may appear surprising to observe large coseismic SE arrivals during the *S*-phase of the wave train (Fig. 1a). However, this apparent contradiction is solved by considering that *SV* waves are also likely to cause volumetric changes by *S*-to-*P* conversion at the Earth's surface and internal interfaces (Fig. 1b).

IRs, sometimes also called 'converted waves', are created when the seismic wave crosses an interface and the electric current balance, binding the coseismic electric field to the seismic wavefield,

© The Author(s) 2019. Published by Oxford University Press on behalf of The Royal Astronomical Society.

Downloaded from https://academic.oup.com/gji/article-abstract/217/1/108/5287972 by Bibliothek des Wissenschaftsparks Albert Einstein user on 08 March 2019

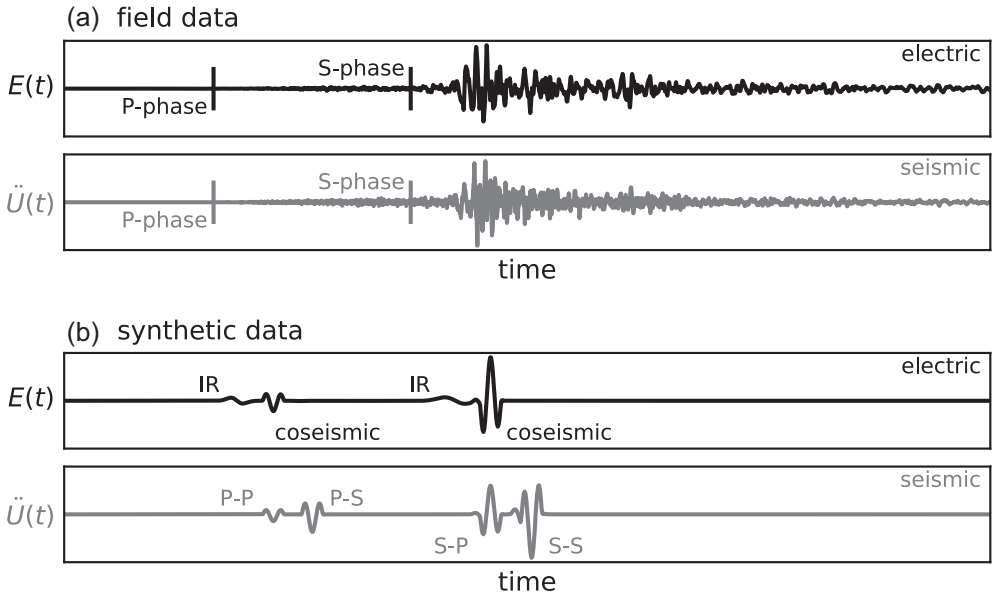

Figure 1. Examples of the main components of the seismoelectric field $E(t)$ and the seismic acceleration $\ddot{U}(t)$: (a) observed waveforms from an M8.1 earthquake at 290-km distance to MT-station, (b) synthetic data for a shallow layer overlying a half-space; coseismic signals are proportional to and concurrent with seismic P waves, IRs appear before and within the seismic wave train.

gets disturbed. The IRs travel with the speed of EM waves and can therefore be detected earlier than the seismic and coseismic signals, from which they were generated. IRs can arrive at the Earth's surface before the seismic first break, but also within the seismic wave train depending on the depth of the interface and the type of the generating wave (Fig. 1b). Like coseismic arrivals, IRs are generated not only from P waves but also from S waves via S-to-P conversion. Furthermore, Zyserman *et al.* (2016) recently showed that IRs, resulting from *SH* waves via induction processes between the magnetic and electric field, can reach significant amplitudes.

IRs are sensitive to porosity, permeability, fluid salinity and fluid viscosity (Garambois & Dietrich 2002) and consequently are of great interest for a hydraulic characterization of the subsoil. SE measurements with artificial sources have shown that IR arrivals can be identified in seismoelectrograms and used for surveying the vadose zone and near-surface aquifers (e.g. Dupuis *et al.* 2007; Strahser *et al.* 2011; Rabbel *et al.* 2019). In these cases, IR arrivals could be detected and digitally processed with multichannel recording by using the very large apparent velocity of IR arrivals on seismoelectrograms as an identification criterion.

In comparison to these near-surface measurements, it is much more difficult to find direct evidence of IR arrivals in earthquake records. This is mainly for two reasons: (1) the electric field is typically recorded with magnetotelluric stations at station spacings too large for array analysis, which is why the apparent slowness of IR arrivals cannot be used as an identification criterion. (2) The amplitudes of IR waves are usually small compared to the ambient noise, which makes detection of IR events difficult even if they precede the seismic first break.

Motivated by the frequent observation of clear SE arrivals from earthquakes on telluric records we have investigated a way to identify IR arrivals despite these difficulties in order to develop their information content for subsurface characterization. The starting point of the considerations presented in the following is that coseismic SE signals and seismic ground acceleration can be expected to be proportional if the theory of Pride (1994) and the low-frequency approximation of Garambois & Dietrich (2001) hold. The factor of proportionality depends only on near-surface soil properties and—in the low-frequency limit—not on frequency. Thus, the presence of IRs in the SE record should lead to deviations from this proportionality and independence of frequency.

SE and seismic field records of signals from natural sources (earthquakes) clearly depend on the source spectra. For making the results of the analysis of different earthquakes comparable to each other the source spectra have either to be accounted for or to be eliminated in the analysis. The latter can be realized without detailed knowledge of the source by forming the ratio of the frequency spectra of the SE and the seismic field records. We name this ratio SESR (SE spectral ratio; Dzieran *et al.* 2019).

The subject of this paper is to quantify the influence of IRs on the SE signals, their spectra and on the SESRs. We have structured the paper in the following way: first, we will explain the concept of the SESRs and their physical significance (Section 2). Next we will present SESRs calculated for three earthquakes from the subduction zone in Northern Chile at three different stations (Section 3). Last, we will present synthetic SESRs derived by forward modelling and inversion to evaluate the SESR approach and investigate the sensitivity of the SESRs with respect to parameter variations of the subsurface (Section 4).

2 SEISMOELECTRIC SPECTRAL RATIOS

SE signals from earthquakes are a mixture of coseismic signals and IRs. To evaluate the influence of the IRs in the signal composition we use the ratio of the electric and seismic amplitude spectra.

For defining the SESR formula we make the following two assumptions:

(1) The horizontal components of the coseismic electric field and ground acceleration, both measured at the Earth's surface, are proportional to each other, according to Garambois & Dietrich (2001).

(2) In the analysis we consider the principal components of the horizontal electric and seismic fields, $E(t)$ and $\ddot{U}(t)$, which are de-

Downloaded from https://academic.oup.com/gji/article-abstract/217/1/108/5287972 by Bibliothek des Wissenschaftsparks Albert Einstein user on 08 March 2019

termined from the recorded horizontal components by polarization analysis and corresponding rotation of sensor coordinate system. In isotropic 1-D layered media, the principal components of both fields would be oriented in the backazimuth direction. In more general types of media the orientations of $E(t)$ and $\ddot{U}(t)$ can disagree. A disagreement can be caused, for example, by fracture systems with a preferred orientation leading to electric and seismic anisotropy. In other words: in using $E(t)$ and $\ddot{U}(t)$ we assume that the proportionality of the horizontal components of the coseismic SE and seismic fields, which is proven for homogeneous media, holds locally for more complicated media, too.

The SE field $E(t)$ and seismic ground acceleration $\ddot{U}(t)$, understood as the respective principal horizontal field components, are the result of the convolution of the respective Green's functions $GE(t)$ and $G\ddot{U}(t)$ with the same source function $SF(t)$. In the frequency domain, the convolution equals a multiplication leading to

$$E(\omega) = GE(\omega) \cdot SF(\omega) \tag{1}$$

$$\ddot{U}(\omega) = G\ddot{U}(\omega) \cdot SF(\omega). \tag{2}$$

The ratio of the SE and the seismic field in the frequency range thus is

$$\mathrm{SESR}(\omega) = \frac{E(\omega)}{\ddot{U}(\omega)} = \frac{GE(\omega)}{G\ddot{U}(\omega)}. \tag{3}$$

With reference to the method of the standard spectral ratio (SSR) first introduced by Borcherdt (1970), we suggest calling this ratio the 'seismoelectric spectral ratio' (SESR).

Coseismic signals are proportional to seismic acceleration, which is why the respective Green's functions and their spectra should follow the same frequency trend. Consequently, if an SE event consisted purely of coseismic signals, the frequency dependency of the two Green's functions as well as the source function should cancel each other out, resulting in a constant SESR. If on the other hand the coseismic signals were mixed with IRs, the SE spectrum would deviate from the coseismic spectrum and the corresponding seismic spectrum leading in this case to a frequency-dependent SESR.

To illustrate this, we computed synthetic seismic and SE spectra for a half-space model that includes an interface 5 km above the source. The receiver for which the spectra are calculated is situated 100 m above the interface in an epicentral distance of 50 km, which means, that the offset is ten times larger than the source depth. For simplicity only the signals related to the fast P wave were included into the calculation. Details of the modelling can be found in Appendix A.

The normalized seismic and SE spectra as well as the corresponding SESRs can be seen in Figs 2(a)–(c). As expected, the seismic spectrum (Fig. 2a) and the coseismic spectrum (Fig. 2b, line II), are proportional to each other, while the SE spectrum including IRs (Fig. 2b, line I) deviates from this form. The resulting SESR of the full SE field therefore shows a decreasing trend, while the SESR from the coseismic field is frequency independent (Fig. 2c, lines I and II).

In the next section, we present SE field data recorded at epicentral distances that are a lot larger than the corresponding earthquakes' source depths. Therefore the question needs to be addressed whether IRs can be expected to be recorded at these offsets. Garambois & Dietrich (2002) showed that IRs are developed over a Fresnel zone that is positioned directly beneath a source located at the Earth's surface. However recent studies suggest that for incident angles larger than the critical angle $\theta_c = \arcsin(v_{seis}/v_{EM})$, so called evanescent IRs are excited (Ren *et al.* 2015, 2018; Butler *et al.* 2018). The evanescent IRs are carried along the interfaces by the seismic waves and can therefore be detected further away from the source. Figs 2(d) and (e) show snapshots of the SE field as well as the IR for the same model configuration that was used to calculate the spectra and SESRs in Figs 2(a)–(c). When comparing Figs 2(d) and (e), one can see that IRs are excited at the locations, where the coseismic waves cross the interface, confirming that the IRs causing the decreasing trend in the SESR is indeed evanescent. Therefore, SESRs are influenced by (evanescent) IRs even at large distances as shown in Fig. 2(c). Furthermore we expect that the shape of the SESRs decrease with increasing frequencies because the amplitudes of evanescent IRs decay approximately with $\exp(-\omega p \Delta z)$, where p is the slowness and Δz the distance between receiver and interface (Ren *et al.* 2018).

In the next section, we present SESRs calculated for three earthquakes recorded on three different stations in Northern Chile to investigate whether our assumptions can in fact be confirmed by the field data.

3 FIELD EXAMPLES

We calculated SESRs for three earthquakes recorded by three different stations (*cf.* Fig. 3 for locations). The M_w 8.1 Pisagua–Iquique earthquake (EQ1) took place on 2014 April 1, and ruptured the central fraction of the Northern Chile–southern Peru seismic gap. A few minutes later a large aftershock of magnitude 6.5 occurred (EQ2). In the early morning of 2014 April 3, the largest aftershock was recorded with a magnitude of 7.6 (EQ3). The ruptures of EQ1 and EQ3 propagated downdip over several tens of seconds with coseismic slips of 4.4 and 1.2 m, respectively. Overall, they broke a segment of 200 km (Schurr *et al.* 2014). Detailed information about the analysed earthquakes can be found in Table 1.

The three earthquakes were, among others, recorded on stations PB01, PB02 and PB09 of the permanent CX-network run by the Integrated Plate Boundary Observatory Chile (IPOC; GFZ & CNRS-INSU, 2006). The stations are equipped with FBA-EST accelerometers, which record the seismic acceleration with a sampling rate of 20 Hz. The electric field is measured by MT-stations along the north–south and east–west directions, also with a 20-Hz sampling rate. This relatively low sampling rate is an advantage as the Nyquist frequency lies at 10 Hz and therefore the SE recordings are not influenced by man-made harmonic noise, such as power lines for example. The electrode dipoles of the MT-stations consist of Ag–AgCl electrodes and have a length of approximately 80 m. Detailed information about the stations are listed in Table 2.

The following steps of data processing were applied to calculate the SESRs:

(1) Correction for instrument response and high-pass filtering: after the instrument response was eliminated from the SE and seismic time-series, a 0.1-Hz high-pass filter was applied to minimize low-frequency influences. To eliminate sporadic anthropogenic bursts the data were despiked before the high-pass filter.

(2) Determination of the principal components of horizontal electric and seismic wavefields: the orientation of the principal components was determined by hodogram analysis. The components were then computed by corresponding rotation of the sensor coordinate system.

(3) Calculation of amplitude spectra and SESR: the amplitude spectra of the seismic and the SE traces were calculated with a fast

Downloaded from https://academic.oup.com/gji/article-abstract/217/1/108/5287972 by Bibliothek des Wissenschaftsparks Albert Einstein user on 08 March 2019

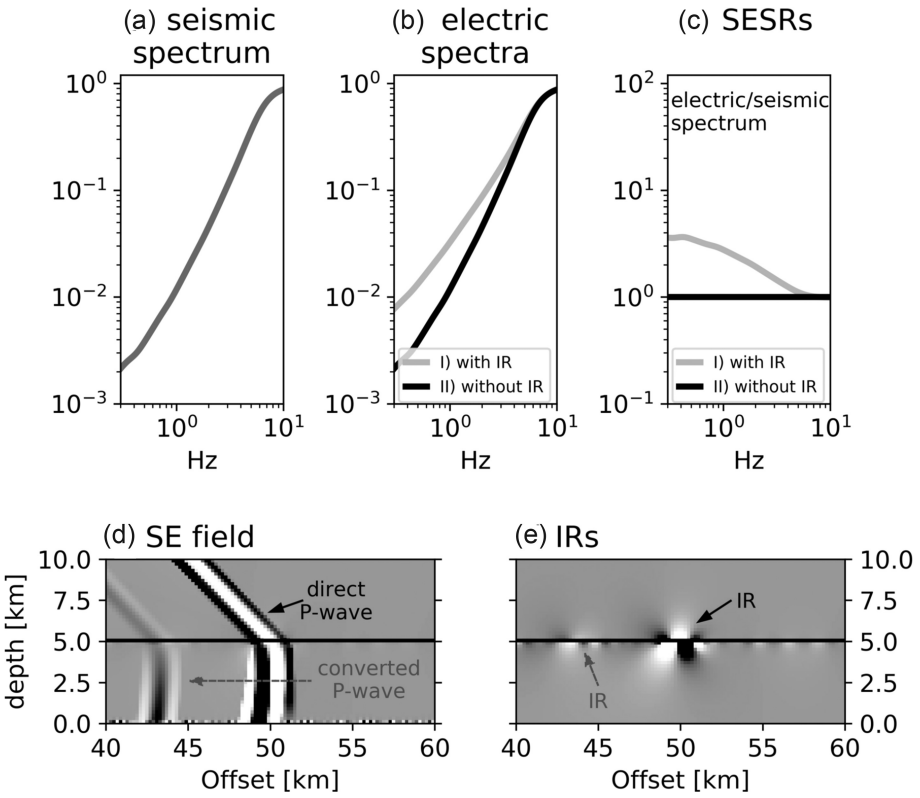

Figure 2. Synthetic calculations for a half-space model including an interface 5 km above the source. The seismic spectrum (a), electric spectra (b) and SESRs (c) were calculated for a receiver at 50-km offset. (d and e) show the corresponding snapshots of the SE field and the IR.

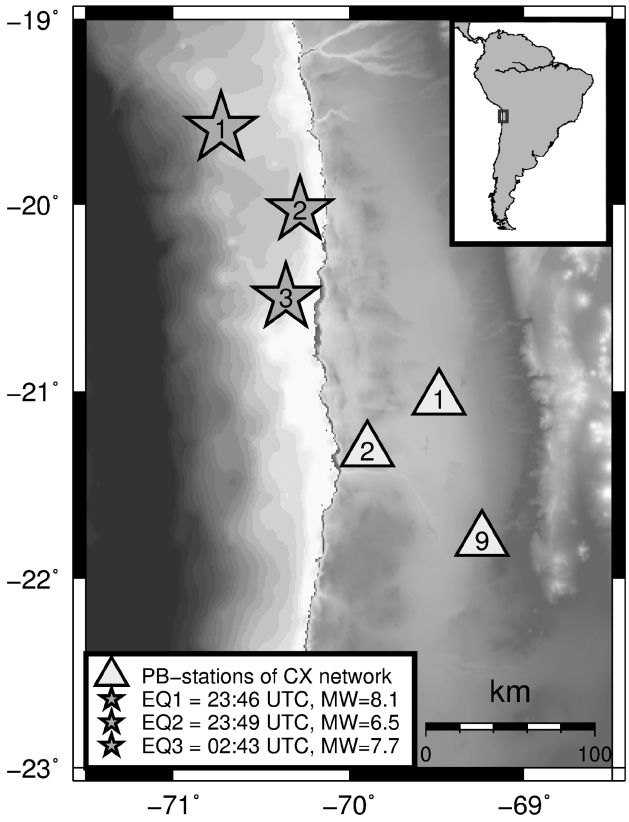

Figure 3. Location of earthquake epicentres and recording stations of the CX-network (IPOC) in Northern Chile presented in this paper.

Table 1. Properties of earthquakes analysed in this paper. Details were provided by the GEOFON Data Centre (1993).

	Time	Latitude	Longitude	Depth	Magnitude
EQ1	2014 April 1 23:46:49	−19.59°	−70.73°	34 km	8.1
EQ2	2014 April 1 23:49:27	−20.03°	−70.28°	16 km	6.5
EQ3	2014 April 3 02:43:17	−20.5°	−70.36°	37 km	7.6

Fourier transformation over a time duration of 150 s. The spectra were smoothed with the Konno–Ohmachi smoothing filter, for which the bandwidth is constant on a logarithmic scale (Konno & Ohmachi 1998). After that, the SESR was calculated as the ratio between the smoothed SE and seismic spectrum.

For the calculation of the SESR, we chose a time window of 150 s. This window includes the *P*- as well as the *S*-phase, which is problematic as the proportionality between the seismic acceleration and SE field is only valid for compressional waves. There are however several reasons why we chose to use the whole wave train. One of them is the low sampling rate of the measured data. If we only included the *P*-phase into our calculations the results would become numerically unstable due to the small number of samples. Additionally, because of the small SE amplitudes in the *P*-phase the signal-to-noise ratio is very low, meaning that the noise could easily influence our results. Lastly, we expect that due to scattering, *SV* and *SH* waves are also present in the *P*-phase and would not entirely be excluded if we restricted ourselves to that part of the wave train.

Downloaded from https://academic.oup.com/gji/article-abstract/217/1/108/5287972 by Bibliothek des Wissenschaftsparks Albert Einstein user on 08 March 2019

Table 2. Location, epicentral distances and electrode distances of the recording stations of the CX-network (IPOC).

Station	Latitude	Longitude	Epicentral distances to EQ1/EQ2/EQ3	Electrode distances (NS/EW)
PB01	−21.0432°	−69.4874°	207 km/139 km/109 km	81.4 m/80.3 m
PB02	−21.3197°	−69.8960°	210 km/148 km/103 km	84.8 m/80.9 m
PB09	−21.7964°	−69.2419°	289 km/223 km/185 km	80.0 m/80.8 m

Figs 4(a)–(c) show the time-series for EQ1, EQ2 and EQ3 on stations PB01, PB02 and PB09, respectively. The earthquakes are easily identified on all records. Compared to the seismic signal strength the electric signal strength is much smaller on stations PB01 and especially PB02 than on station PB09, showing that the transfer functions between the SE and electric field are site-dependent.

The SESRs were calculated for all earthquakes on each station (Fig. 4d). They all show a decreasing trend with increasing frequencies. Additionally, a great similarity can be found between SESRs on the same station. To compare the SESRs between the stations we calculated an average SESR for each location (Fig. 5). This reveals that although all SESRs share a similar tendency, the trend differs between the stations. On stations PB01 and PB09, the SESRs decrease equally up to 0.3 Hz. Above that frequency the gradients of the two slopes stay similar but the amplitude of the average SESR at station PB01 is higher than that at station PB09. At 4 Hz, the decrease of the SESR at station PB01 stops, so that the SESR appears almost flat above that frequency. Between 0.2 and 1.4 Hz the decrease of the SESR at station PB02 is slightly steeper than on stations PB01 and PB09, although above 1.4 Hz the rate of the decay is also decreasing.

The field data show that the SESRs are consistent for different earthquakes at the same station but differ among locations. The decreasing trend of the SESRs shows that the transfer function between seismic and SE signals depends strongly on frequency, which is in contrast to the frequency independence that is expected for pure coseismic signals. The agreement of the SESRs at each station in combination with the differences of SESRs between locations shows that the SESRs are probably more influenced by site effects than by actual earthquake characteristics. This supports our idea that IRs are causing the decreasing trends of the SESRs, although other effects should not be entirely excluded.

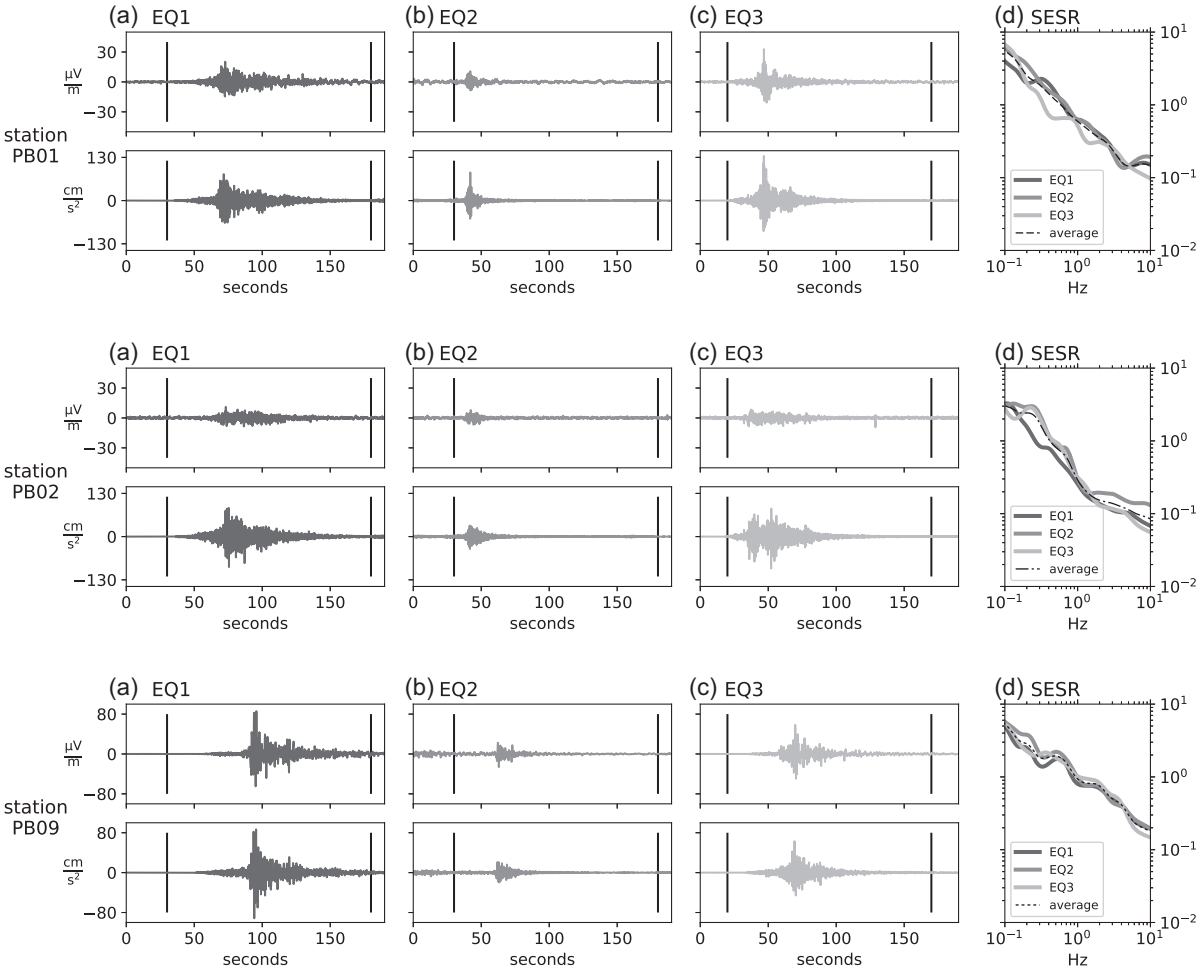

Figure 4. (a–c) Electric and seismic traces of EQ1–EQ3 recorded at stations PB01, PB02 and PB09. The SESR spectra were calculated for the data between the vertical black lines; (d) log–log plots of the SESRs of the data presented in panels (a)–(c).

Downloaded from https://academic.oup.com/gji/article-abstract/217/1/108/5287972 by Bibliothek des Wissenschaftsparks Albert Einstein user on 08 March 2019

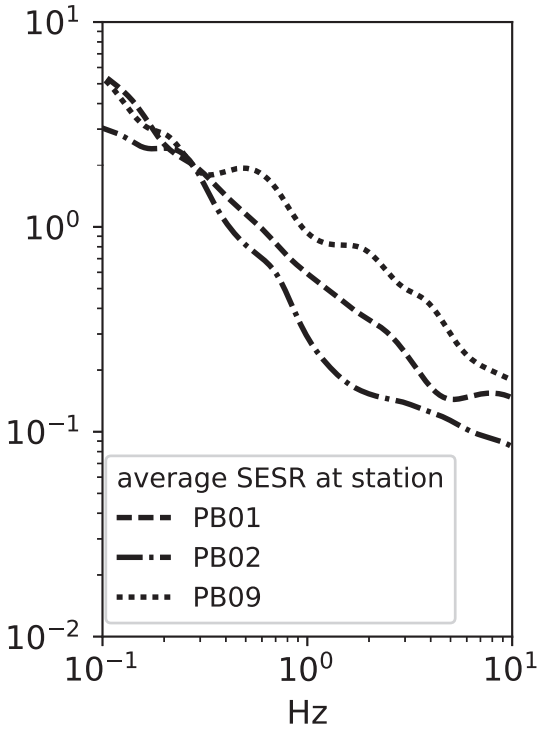

Figure 5. The average SESRs of stations PB01, PB02 and PB09, derived from the SESRs of EQ1–EQ3 (Fig. 4).

Due to their fast attenuation, we expect that the IRs observed at the Earth's surface have to be excited in close vicinity to the recording stations as otherwise they would not influence the SE signals. The example calculated for a half-space model in Section 2 showed that we can expect evanescent IRs to influence SESRs recorded at large offsets (Fig. 2). The question is, how close to a station the IRs have to be excited to influence the SESRs significantly, considering that this is an M_w 8.1 megathrust earthquake. In the next section, we therefore use synthetic data to evaluate our interpretation of the field data SESRs.

4 MODELLING

4.1 Modelling and SESR calculation

The numerical modelling was performed with a Fortran code developed by Garambois & Dietrich (2002) and extended by Warden *et al.* (2013) for unsaturated media. Based on the general reflectivity method the code models seismo-EM wave propagation in stratified media excited by point forces. We used the code to calculate the spectral Green's functions (impulse-type point source) of the seismic and SE fields in an *x*,*y*,*z*-Cartesian coordinate system, with *z* pointing downwards. To investigate the IR contributions to the total signal we used the ability of the code to manually suppress the computation of IRs at selected interfaces and the free surface.

As an example, we chose to model the average SESR of station PB09 (Fig. 5), which we will further refer to as observed SESR. To obtain the corresponding modelled SESR, we calculated the seismic and SE Green's functions for a point force directed in *z*-direction. We chose the point force orientated in the vertical direction, as we inferred from the SE traces (Figs 4a–c) that the *S*-phase is more prominent than the *P*-phase, which corresponds to the radiation pattern of the *P*- and *S*-phases from a vertical point force. The point force is located at 25-km depth and the receiver is positioned at the surface at a distance of 135 km in *x*-direction and −190 km in *y*-direction, which is roughly the epicentre of EQ1–EQ3.

We calculated the Green's functions for a time duration of 409.6 s with a sampling rate of 20 Hz, which is similar to the sampling rate of the field data. The Green's functions were smoothed as described in Section 3 and then divided to calculate the SESRs.

The parameters of our subsurface model are based on a seismic velocity model of Sick *et al.* (2006) and an electric resistivity model of Vargas (2016), both developed for the region around station PB09. For modelling the site effect we inserted two shallow sedimentary layers at the surface. By manually modifying the depth, porosity and salinity of the upper three layers we gradually adjusted the form of the modelled SESR to that of the observed SESR. We restricted ourselves to altering the uppermost soil properties as first tests revealed that the shape of the modelled SESR was most sensitive to the parameters in this depth range. The main input parameters of our final model as well as resulting subsurface properties are listed in Table 3 and shown in Fig. 6. Depth, porosity, permeability and fluid salinity values are direct input parameters, while the velocities and resistivity are calculated by the program. We assumed full saturation for all layers except the first, where we lowered the saturation to 75 per cent. The detailed input parameters for our calculations can be found in Table B1 in the appendix.

4.2 Influence of interface responses

The modelled SESR agrees well with the observed SESR in the major part of the considered frequency interval (compare lines a and b in Fig. 7). A few deviations can be seen, especially for frequencies below 1.5 Hz, but the overall trend is well fitted. Thus we decided to use this model as a basis for further calculations.

To find out whether the shape of the SESR is influenced by IRs we calculated a comparative coseismic SESR without any IR (Fig. 7, line c). As expected, the resulting SESR is flat showing no significant frequency dependency. This proves that IRs are in fact responsible for the decreasing trend of the SESR.

When thinking about possible applications, it is necessary to know at which depth the IRs that influence the shape of the SESR are excited. We therefore calculated SESRs based on the same model, successively allowing IRs to be created at deeper interfaces. When IRs are only allowed from the interface at 100-m depth the SESR deviates significantly from the SESR calculated with IRs from all interfaces (compare lines a and d in Fig. 8). However, when allowing IRs from interfaces at 100- and 300-m depth, only a small deviation between that SESR and the original one can be seen in the low frequency range (compare lines b and d in Fig. 8). This shows that, at least for this model, the shape of the SESR is primarily influenced by the IRs created at the 100- and 300-m deep interfaces. To verify this conclusion we calculated the SESR for an SE field that only allows IRs created at interface deeper than 300 m (line c in Fig. 8). As expected, this SESR deviates from the coseismic SESR shown in Fig. 7 (line c) by a few per cent only and for frequencies smaller than 0.6 Hz. This confirms that the SESR is majorly influenced by the parameters in the upper three layers.

4.3 Influence of model parameters

Next we analyse the sensitivity of the SESR with respect to the different input parameters of the model. Garambois & Dietrich (2002) showed that porosity, permeability, fluid salinity and fluid

Downloaded from https://academic.oup.com/gji/article-abstract/217/1/108/5287972 by Bibliothek des Wissenschaftsparks Albert Einstein user on 08 March 2019

Table 3. Main properties of the layers used for modelling the average SESR of station PB09. The properties of the first three layers (⋆) were varied to adjust the form of the modelled SESR to that of the observed SESR. Depth, porosity, permeability and fluid salinity are input parameters; velocities and resistivity are calculated by the program (marked with ∗).

Layer	1⋆	2⋆	3⋆	4	5	6	7	8
Depth (km)	0.1	0.3	2.5	7.0	22.0	37.0	50.0	>50
Porosity (per cent)	20	5.0	1.0	0.5	0.1	0.1	0.1	0.1
Permeability (Darcy)	0.1	0.1	0.1	0.01	0.01	0.01	0.01	0.01
Fluid salinity (mol l^{-1})	0.0095	0.014	0.013	0.3	1	1	1	1
$*v_P$ (km s^{-1})	1.87	2.57	3.5	6.0	6.4	6.8	7.0	8.0
$*v_S$ (m s^{-1})	1.00	1.51	2.02	3.47	3.69	3.93	4.04	4.62
$*v_{EM}$ at 2 Hz (km s^{-1})	25.8	43.5	128.7	71.4	130.8	130.8	130.8	130.8
∗Resistivity (Ωm)	134	378	3302	1016	3409	3409	3409	3409

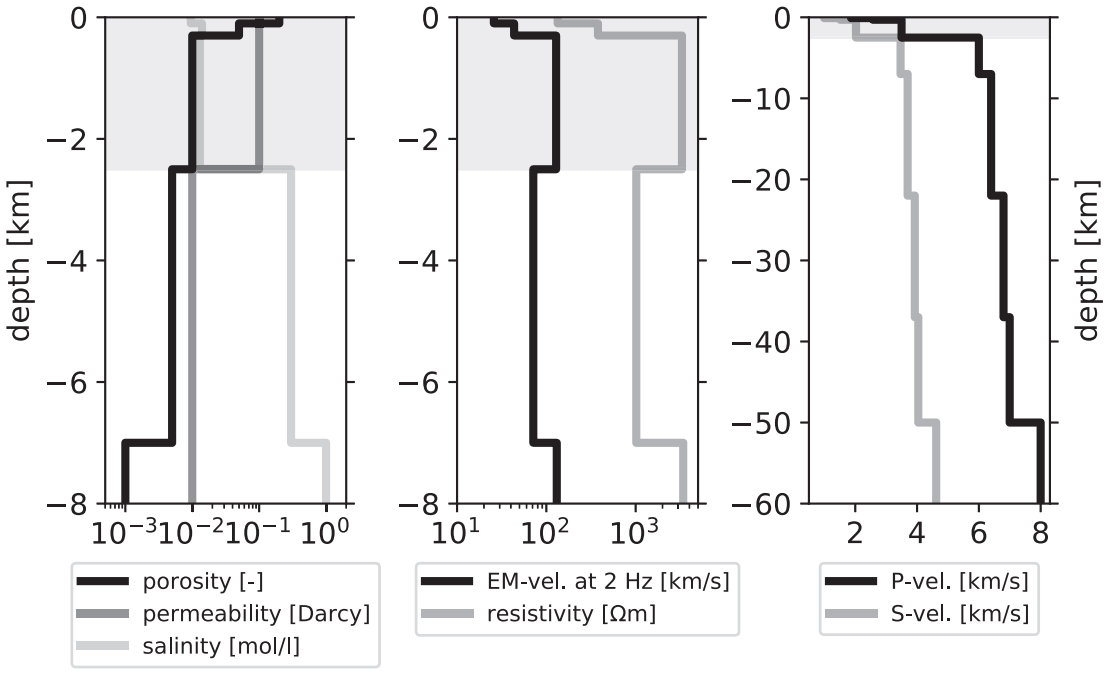

Figure 6. Layer properties used to model the SESR. The properties in the upper three layers (shaded area) were varied to adjust the behaviour of the modelled SESR to that of the observed SESR. Porosity, permeability and fluid salinity are input parameters; velocities and resistivity are calculated by the program. The values are constant outside of the displayed depth range.

viscosity have the strongest influence on the amplitudes of a single shallow IR. As in our model only the first three layers contribute relevantly to the IR signals, we calculated the sensitivity for these layers with respect to porosity, permeability, fluid salinity and depth, which from now on refers to the depth of the lower interface of the layer. The fluid viscosity was assumed to be constant.

Each of the parameters was varied independently by ±1 per cent. The relative change of the SESR at each frequency $\Delta S(\omega)$ was then calculated via

$$\Delta S(\omega)_p = \frac{S_p^{+1\%}(\omega) - S_p^{-1\%}(\omega)}{2 \cdot S(\omega) \cdot 1\%}, \tag{4}$$

where $S(\omega)$ is the original SESR and $S_p^{\pm 1\%}(\omega)$ the SESR resulting from the variation of parameter p.

Fig. 9 shows the results of the parameter variation. Although all parameter changes show a clear frequency dependency, no predominant trend can be seen. Except for the salinity in the third layer all parameter variations lead to positive as well as negative effects on the shape of the SESR regarding different frequency bands.

Overall, the SESRs do not vary more than 2 per cent from their original form, except for the depth of layer 3 (interface at 2500 m). Here the deviation of 1 per cent leads to an SESR change of up to 5 per cent. The permeability, with a sensitivity of less than 0.2 per cent, has the least influence on the shape of the SESRs. This seemingly small effect can be explained by the low percentage (1 per cent) by which the permeability is varied. Garambois & Dietrich (2002), for example, varied the permeability by factor 10 in their study, which would consequently result in larger effects.

In the case of porosity and salinity, the calculations show that the sensitivity decreases for deeper interfaces. Additionally, the effects of the parameter variation generally become larger for frequencies above 1 Hz. However, the sensitivity to permeability behaves differently. Not only is it stronger in the low-frequency range (below 1 Hz) but the permeability in the deepest layer (considered layer 3) also seems to affect the SESR the most. One explanation for the increased sensitivity in the third layer could be that contrary to the two upper layers there is already an existing permeability contrast between layers 3 and 4 (0.1–0.01 Darcy), which is enlarged even further by the parameter variation.

Another surprising result is the sensitivity of the response of the third layer with respect to depth, considering that the IRs from this interface should not influence the SESR at all (Section 4.2). This

Downloaded from https://academic.oup.com/gji/article-abstract/217/1/108/5287972 by Bibliothek des Wissenschaftsparks Albert Einstein user on 08 March 2019

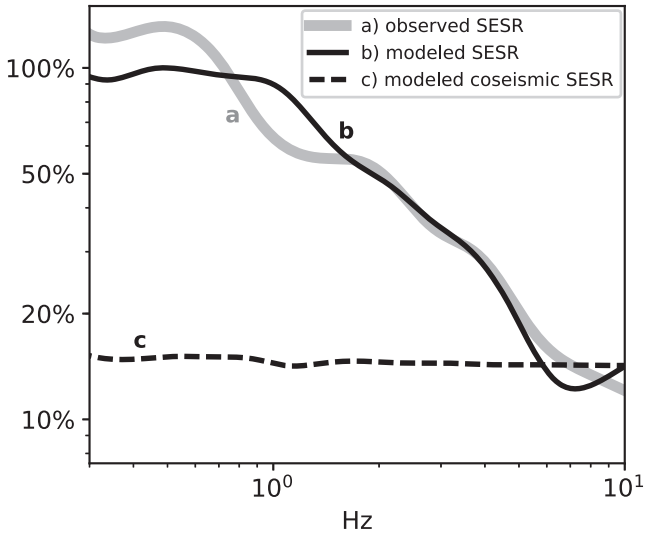

Figure 7. Comparison of the observed and modelled SESRs. (a) Observed SESR, (b) modelled SESR including IRs at all interfaces and (c) modelled SESR of coseismic field (no IRs). The modelled SESRs (lines b and c) were calculated with the same input parameters. All SESRs are normalized to the maximum of the modelled SESR (line b).

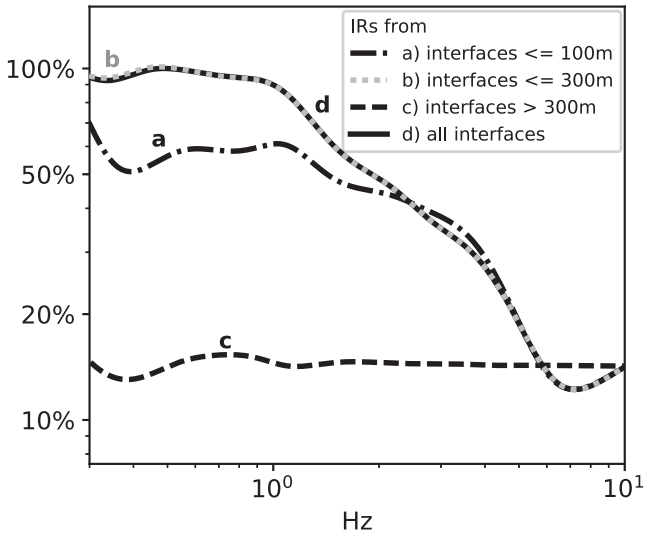

Figure 8. Comparison of SESRs with IRs being included sequentially for each interface. (a) SESR including only IRs from interface at 100 m, (b) SESR including only IRs from interfaces at 100 and 300 m, (c) SESRs including only IRs from interfaces at 2500 m and deeper and (d) SESRs including IRs from all interfaces. All SESRs are normalized to the maximum of the modelled SESR (line d).

effect can be explained by the fact that the sensitivity to the depth of the layer is, in this case, not related to the IRs themselves, but rather caused by differing travel paths of the seismic waves, resulting in wavefield variations. This shows that the absolute depth of the layer interfaces may have a relatively larger impact on the result than the material parameters themselves. This problem will be further addressed in Section 5.

4.4 Inversion

Having calculated the sensitivities of the SESRs to different parameters and layers, the next step is to implement an inversion algorithm to see whether it is possible to improve our model. For our inversion attempt we decided to use an iterative linearized inversion based on the Levenberg–Marquardt algorithm (Lines & Treitel 1984).

The SESR S_f is a function of the rock properties m_p of the subsurface where the indices $f = 1, ..., n_f$ and $p = 1, ..., n_p$ indicate single frequencies and model parameters, respectively:

$$S_f = \mathcal{F}(m_p). \tag{5}$$

We assume that the observed and initially modelled SESR are similar. Then it is possible to express the observed SESR S_f^{obs} by a Taylor series expansion of $\mathcal{F}(m_p)$ around the modelled SESR S_f^{mod} and neglect the higher order terms.

$$S_f^{\text{obs}} \approx S_f^{\text{mod}} + \left.\frac{\partial S_f^{\text{mod}}}{\partial m_p}\right|_{m_p^{\text{mod}}} \Delta m_p. \tag{6}$$

Since we linearize the Taylor series expansion, we are using an iterative approach to gradually adjust the subsurface parameters:

$$S_f^{\text{obs}} \approx S_f^{i-1} + \left.\frac{\partial S_f^{i-1}}{\partial m_p}\right|_{m_p^{i-1}} \Delta m_p^i \qquad for\ i = 1, ..., n_i, \tag{7}$$

where m_p^{i-1} are the subsurface parameters at the $(i-1)$th iteration and S_f^{i-1} is the corresponding SESR. Following that, $m_p^i = m_p^{i-1} + \Delta m_p^i$ are the adjusted parameters after the ith iteration resulting in the SESR S_f^i. The series of the modelled S_f^i is supposed to converge towards the observed S_f^{obs}. The subsurface parameters for the starting model m_p^0 are listed in Table B1 and the corresponding SESR S_f^0 can be seen in Fig. 7 (line b).

$(S_f^{\text{obs}} - S_f^{i-1})$ and Δm_p^i are normalized to express eq. (7) in fraction:

$$\frac{S_f^{\text{obs}} - S_f^{i-1}}{S_f^{i-1}} \approx \left(\left.\frac{\partial S_f^{i-1}}{\partial m_p}\right|_{m_p^{i-1}} \frac{m_p^{i-1}}{S_f^{i-1}}\right)\left(\frac{m_p^i - m_p^{i-1}}{m_p^{i-1}}\right). \tag{8}$$

Eq. (8) is then expressed in terms of the data vector d_f^i, the kernel $G_{f,p}^i$ and the model vector $\Delta\tilde{m}_p^i$:

$$d_f^i = \frac{S_f^{\text{obs}} - S_f^{i-1}}{S_f^{i-1}}, \tag{9}$$

$$G_{f,p}^i = \left(\left.\frac{\partial S_f^{i-1}}{\partial m_p}\right|_{m_p^{i-1}} \frac{m_p^{i-1}}{S_f^{i-1}}\right) = \Delta S_{f,p}, \tag{10}$$

$$\Delta\tilde{m}_p^i = \left(\frac{m_p^i - m_p^{i-1}}{m_p^{i-1}}\right). \tag{11}$$

d_f^i can easily be calculated. $\Delta S_{f,p}$ is the change in the SESR at frequency f with respect to parameter p as defined in eq. (4). With this, the components of the model vector $\Delta\tilde{m}_p^i$ can be determined in a least-squares sense solving eq. (8) via the Levenberg–Marquardt algorithm:

$$\Delta\tilde{m}_p^i = ((G_{f,p}^i)^T G_{f,p}^i - \beta I_{f,p}^i)^{-1}(G_{f,p}^i)^T d_f^i, \tag{12}$$

where β is the Levenberg–Marquardt damping parameter and $I_{f,p}^i$ the unit matrix.

Following this, the subsurface parameters can be updated via

$$\begin{aligned} m_p^i &= m_p^{i-1} + \frac{m_p^i - m_p^{i-1}}{m_p^{i-1}} m_p^{i-1} \\ &= m_p^{i-1}\left(1 + \Delta\tilde{m}_p^i\right), \end{aligned} \tag{13}$$

Downloaded from https://academic.oup.com/gji/article-abstract/217/1/108/5287972 by Bibliothek des Wissenschaftsparks Albert Einstein user on 08 March 2019

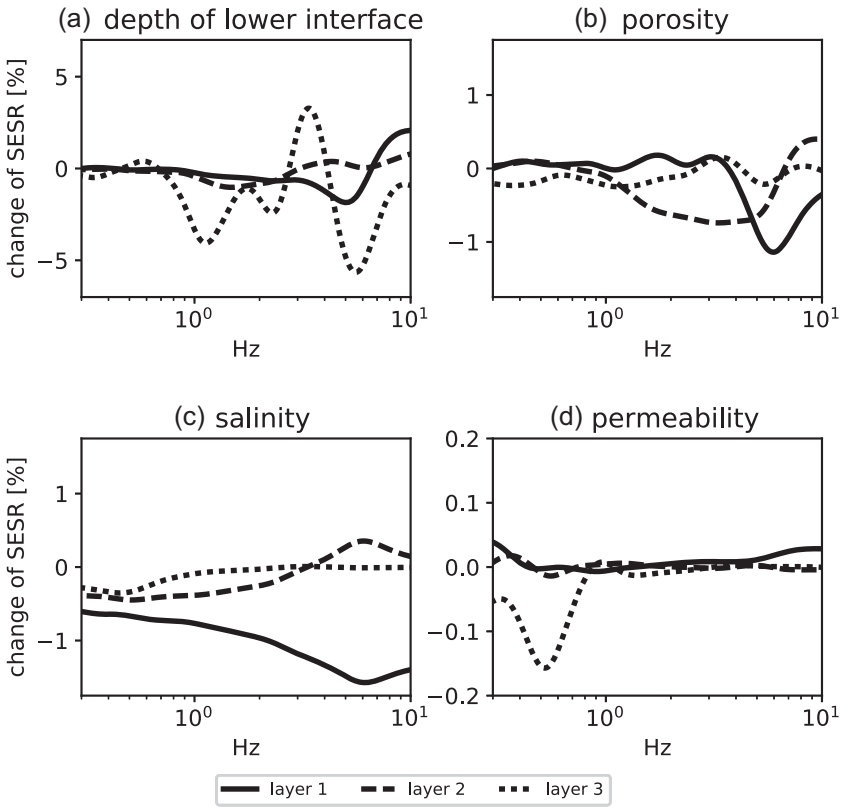

Figure 9. Sensitivity analysis: change of the SESR in per cent if (a) depth of the lower interface, (b) porosity, (c) salinity and (d) permeability in layers 1–3 are increased by 1 per cent.

from which we can compute the new SESR via $S_f^i = \mathcal{F}(m_p^i)$.

The new residuals of the data can then be calculated as

$$\tilde{d}_f = \frac{S_f^{\text{obs}} - S_f^i}{S_f^{i-1}}, \tag{15}$$

where the quality of the fit is measured by the rms value

$$\Delta d_{\text{rms}} = \sqrt{\frac{\sum_f (\tilde{d}_f)^2}{n_f}}. \tag{16}$$

We tried different damping factors for our inversion. We finally chose a damping factor of $\beta = 5$ as this led to the smallest possible Δd_{rms} without resulting in unreasonable subsurface parameters. With $\beta = 5$ the inversion was terminated after six cycles during which the rms value Δd_{rms} decreased by 43 per cent.

Fig. 10 shows the resolution matrix for the first inversion. It reflects the result of the sensitivity analysis (Section 4.3). Together with the salinity of the first layer the depth of interfaces influence the SESR the most. While the sensitivity with respect to porosity and salinity decreases with depth, changes in the permeability seem to be insignificant. A lower β-value could enhance the influence of the permeability. Unfortunately, in our test run, this led to negative salinity values that are not realistic. We therefore decided not to further decrease β.

Table 4 lists the adjusted depths, porosities, permeabilities and fluid salinities of the inverted model as well as the resulting velocities and resistivities. All other input parameters remained constant and can be found in Table B1. The depth of the layers were changed by less than 6 per cent. This is surprising as the sensitivity analysis as well as the resolution matrix suggested a high influence of

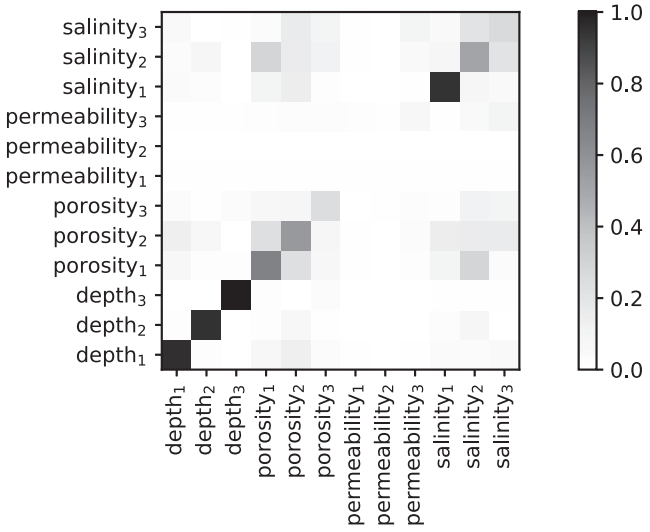

Figure 10. Resolution matrix for $\beta = 5$; The parameters' subscript number corresponds to the respective layer.

the interface positions. Larger variations can be found for porosity, permeability and salinity. The largest adjustments to the porosity were made in the uppermost layer (−50 per cent), while the permeability and salinity were changed most in the third layer (−39 and −78 per cent). This is plausible, as the sensitivity analysis suggests that variations of permeability and salinity in the third layer affect mostly lower frequencies, which is where the biggest discrepancy

Downloaded from https://academic.oup.com/gji/article-abstract/217/1/108/5287972 by Bibliothek des Wissenschaftsparks Albert Einstein user on 08 March 2019

Table 4. Major properties and the change in per cent of the upper three layers after the inversion compared to the original model. Depth, porosity, permeability and fluid salinity are input parameters; velocities and resistivity are calculated by the program (marked with ∗).

Layer	1	2	3
Depth (km)	0.096 (−4 %)	0.297 (−1 %)	2.64 (+6 %)
Porosity (per cent)	10 (−50 %)	3.1 (−39 %)	1.28 (−28 %)
Permeability (Darcy)	0.087 (−13 %)	0.098 (−2 %)	0.061 (−39 %)
Fluid salinity (mol l^{-1})	0.012 (+26 %)	0.010 (−26 %)	0.003 (−78 %)
$*v_P$ (km s^{-1})	2.18 (+16 %)	2.62 (+2 %)	3.49 (−0.3 %)
$*v_S$ (km s^{-1})	1.22 (+22 %)	1.56 (+3 %)	2.01 (−0.5 %)
$*v_{EM}$ at 2 Hz (km s^{-1})	36.2 (+40 %)	70.1 (61 %)	232.8 (+81 %)
∗Resistivity (Ωm)	263 (+97 %)	979 (159 %)	10835 (+228 %)

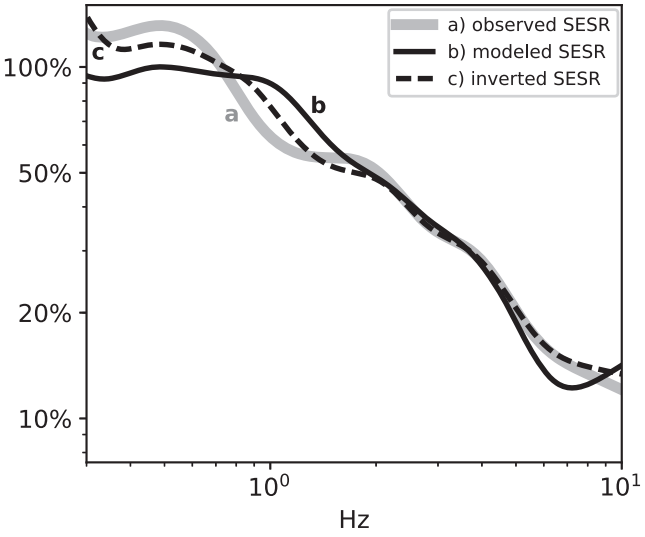

Figure 11. Comparison of the observed SESR (a) with the modelled SESR before (b) and after the inversion (c). The SESRs are normalized to the maximum of the modelled SESR (line b).

between the observed and modelled SESR were found. When looking at the subsurface parameters that are not direct model inputs but calculated by the program one can see that the seismic velocities are mostly affected in the first layer (+22 per cent), possibly due to the large porosity change. The highest variations can be found in the resistivity (over 100 per cent). This is reasonable as the resistivity of the layers has a direct impact not only on the creation of the IRs but also on the propagation of the EM waves due to damping and velocity effects.

Fig. 11 compares the observed SESR (line a) to the originally modelled SESR (line b) and the modelled SESR after the inversion (line c). Above 2 Hz, the inverted SESR now represents the observed SESR very well. Below 2 Hz, the model was also improved but deviations are still visible. These could possibly be minimized by adding another layer or using a more advanced inversion algorithm, which we leave to a future study.

In summary, we were able to show that in principle it is possible to fit modelled and measured SESRs via forward modelling and linearized inversion using simplifying subsurface models and assumptions. One has to consider though that IRs and therefore SESRs are influenced by different parameters in a variety of ways, which complicates the validation of the solution. However, if additional geophysical measurements can provide prior subsurface information (as for example seismic velocities, densities and interface depths), SESRs could be a suitable method to derive information about parameters like porosity or permeability in the upper subsurface.

5 DISCUSSION

5.1 Importance of model geometry

In this paper, we introduced SESRs as a concept to quantify the influence of IRs on SE signals and their spectra independently of the earthquake source spectrum. For the synthetic studies we decided to focus on the subsurface parameters of the shallow layers rather than the geometry of the model including, for example, layer depths or the source position. Nevertheless, these characteristics should not be neglected in a thorough investigation.

The sensitivity analysis (Section 4.3) as well as the resolution matrix of the inversion (Fig. 10) show that the depth of the third layer has a large influence on the SESRs even though the IRs that are excited at this interface do not (Section 4.2). We therefore calculated the sensitivities of the SESR towards all layer depths as well as the depth of the source and found that each of these parameters can influence the resulting SESR. We suspect differing wave paths to be a reason for this as they result in varying reflection and transmission angles in the upper layers. It is therefore important to have a realistic estimate of the subsurface layer structure or to include these parameters into the inversion.

Beside the layer and source depth we evaluated the importance of choosing the appropriate source orientation. For this we recalculated our model with a point force orientated in the *y*- instead of the *z*-direction. For both source orientations we then calculated the SESRs once including only the *P*-phase and once the whole wave train, resulting in four different SESRs (Fig. 12). When comparing the SESRs calculated from the *P*-phase only, no large differences can be seen between the SESRs computed from the vertical and horizontal point force (compare lines a and b). Yet, when the whole wave train is included into the calculation, the deviation becomes obvious (compare lines c and d). We therefore infer from Fig. 12 that if one restricts oneself to the *P*-phase for the SESR calculation, the source orientation can be neglected. If on the other hand, the whole wave train is used, the source model has to be taken into account.

Lastly we verified whether the source strength has an influence on the SESRs. At least for our calculations this did not seem to be the case. It seems as if the IRs, the coseismic and the seismic field all depend on the source strength equally, which means that the difference gets cancelled out when the ratio is calculated.

Downloaded from https://academic.oup.com/gji/article-abstract/217/1/108/5287972 by Bibliothek des Wissenschaftsparks Albert Einstein user on 08 March 2019

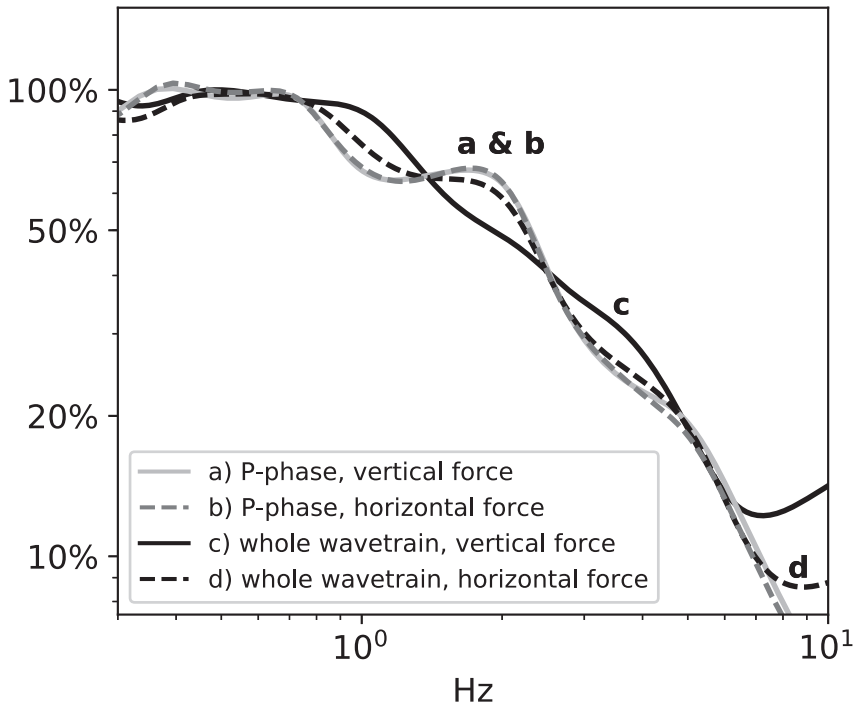

Figure 12. SESRs calculated from the *P*-phase (lines a and b) and the whole wavefield (lines c and d) for a vertical and a horizontally orientated force (lines a and c and lines b and d).

5.2 SESRs as a monitoring tool?

A possible application of SESRs derived from earthquake data may be the attempt to observe changes of subsurface parameters over time. This raises the question of the accuracy, with which SESRs can be expected to be determined, in relation to the magnitude of possible changes of the SESR by variation of relevant subsurface parameters. A general answer clearly requires an extensive numerical investigation. However, a first guess may be derived already from the results of this study. The SESRs calculated from the field data recorded at station PB09 (Fig. 4d) deviate from the average SESR about roughly 15 per cent. This value may be seen as an order of magnitude of what may be expected under favourable noise conditions (*cf.* Dzieran *et al.* 2019 regarding the influence of noise on the detectability of SESRs). It defines the order of magnitude which needs to be exceeded by SESR variations caused by varying subsurface parameters. From the sensitivity analysis (Fig. 9) we can conclude that the porosity or salinity would have to change by more than 15 per cent to be reliably identifiable and the permeability should undergo changes of at least 2 decades. While these values appear rather large, some scenarios can be thought of that might lead to said changes, as for example, crack openings or sudden fluid intrusions in tectonically or volcanically active environments. Clearly, it may be difficult to distinguish whether one single parameter or a combination of parameters is responsible for possibly observed changes in the SESR.

5.3 Limitations of SESR concept

The SESR concept is based on the assumption that the coseismic SE field and the ground acceleration are proportional (Section 2). In that case, the spectra of the coseismic field and the seismic acceleration should also be proportional and a frequency dependency should only be caused by IRs. During our computations however, we found that for small epicentral distances this assumption might not hold. For epicentral distances smaller than the source depth a frequency-dependent behaviour could be observed in the SESRs even in the case of a purely coseismic field. We believe that conversions from *P*-to-*S* energy (and the other way round) at the free surface might be a possible reason, but further investigation is definitely necessary.

An additional problem might be the noise level on the data. The noise could influence the seismic and electric spectra differently. This can lead to an additional frequency-dependent disturbance of the SESR that is not caused by IRs. A further factor that influences the SESRs could be the sensor coupling with the subsurface. We therefore highly recommend to check (e.g. through modelling) whether a proportionality between the seismic and electric noise fields can be assumed before evaluating SESRs towards the influence of IRs.

5.4 Future prospects

In this paper, we introduced SESRs as a new concept. We are aware that before being able to reliably use SESRs to study the subsurface a lot more research needs to be conducted in both numerical studies and field applications. Data quality and the influence of noise, for example, needs to be investigated as well as possible model ambiguities.

By rotating the data into their principal component we have reduced the problem to 1-D. One could however also consider a vectorial approach to calculate an SESR tensor for considering 3-D effects and anisotropy.

Furthermore one could think about applying SESRs not only to earthquake studies but investigate whether the method can be transferred to active source SE exploration applications as well.

In any case, we are confident that SESRs can be used to help to determine hydrologically relevant subsurface parameters *in situ*.

Downloaded from https://academic.oup.com/gji/article-abstract/217/1/108/5287972 by Bibliothek des Wissenschaftsparks Albert Einstein user on 08 March 2019

6 CONCLUSION

To quantify the influence of IRs on SE signals caused by earthquakes and their spectra we introduced the concept of SESRs. Analysis of both numerical and field data showed that the presence of IRs causes a frequency dependency of the ratio of the electric and seismic spectra. In particular, the field data analysis showed that the form of frequency dependence of the SESRs is site specific: it depends mainly on the hydrogeophysical structure underneath the recording station. Numerical modelling showed that the IRs influencing the SESR are created in the upper few hundred metres of the subsurface. Considering a geologically realistic range of parameter variation, we found that changes in salinity and porosity may influence SESRs more than the hydraulic permeability. The variation of the SESRs caused by the variation of different subsurface parameters is frequency-dependent, too, in a complicated way. Therefore, inversion algorithms need to be applied for recovering subsurface parameter variations from SESRs. Based on a given regional seismic crustal model and realistic hydrogeophysical parameters we showed that the observed SESRs can be reproduced by forward modelling and linearized inversion.

ACKNOWLEDGEMENTS

First of all, we would like to thank the reviewers for their constructive comments. The field data were acquired in the framework of the IPOC Project. The authors would like to thank Jaime Araya Vargas for making the MT-data available. The data used in this paper can be requested from the authors. The station map (Fig. 3) was created with Generic Mapping Tools software (Wessel *et al.* 2013) and the data analysed with ObsPy (Krischer *et al.* 2015). The first author is grateful for funding through a scholarship of the Christian-Albrechts-Universität zu Kiel ('Landesgraduiertenstipendium').

REFERENCES

Biot, M.A., 1956. Theory of propagation of elastic waves in a fluid-saturated porous solid. I. Low-frequency range, *J. acoust. Soc. Am.,* **28**(2), 168–178.

Biot, M.A., 1962. Mechanics of deformation and acoustic propagation in porous media, *J. Appl. Phys.,* **33**(4), 1482–1498.

Borcherdt, R.D., 1970. Effects of local geology on ground motion near San Francisco bay, *Bull. seism. Soc. Am.,* **60**(1), 29–61.

Bordes, C., Sénéchal, P., Barrière, J., Brito, D., Normandin, E. & Jougnot, D., 2015. Impact of water saturation on seismoelectric transfer functions: a laboratory study of coseismic phenomenon, *Geophys. J. Int.,* **200**(3), 1317–1335.

Butler, K.E., Kulessa, B. & Pugin, A.J., 2018. Multi-mode seismoelectric phenomena generated using explosive and vibroseis sources, *Geophys. J. Int.,* **213,** 836–850.

Dupuis, J.C., Butler, K.E. & Kepic, A.W., 2007. Seismoelectric imaging of the vadose zone of a sand aquifer, *Geophysics,* **72**(6), A81–A85.

Dzieran, L., Rabbel, W., Thorwart, M. & Ritter, O., 2019. Seismoelectric ground response to local and regional earthquakes, in *The Seismoelectric Effect: Theory, Numerical Modeling, Laboratory and Field Experiments,* eds Grobbe, N., Revil, A., Zhu, Z. & Slob, E., Wiley Online Library, in press.

Frenkel, J., 1944. To the theory of seismic and seismoelectric phenomena in saturated soil, *Izv. Acad. Nauk USSR,* **8**(4, 230–241).

Gao, Y. & Hu, H., 2010. Seismoelectromagnetic waves radiated by a double couple source in a saturated porous medium, *Geophys. J. Int.,* **181,** 873–896.

Gao, Y., Chen, X., Hu, H., Wen, J., Tang, J. & Fang, G., 2014. Induced electromagnetic field by seismic waves in Earth's magnetic field, *J. geophys. Res.,* **119**(7), 5651–5685.

Gao, Y., Harris, J.M., Wen, J., Huang, Y., Twardzik, C., Chen, X. & Hu, H., 2016. Modeling of the coseismic electromagnetic fields observed during the 2004 M_w6.0 Parkfield earthquake, *Geophys. Res. Lett.,* **43**(2), 620–627.

Garambois, S. & Dietrich, M., 2001. Seismoelectric wave conversions in porous media: field measurements and transfer function analysis, *Geophysics,* **66**(5), 1417–1430.

Garambois, S. & Dietrich, M., 2002. Full waveform numerical simulations of seismoelectromagnetic wave conversions in fluid-saturated stratified porous media, *J. geophys. Res.,* **107**(B7), ESE 5–1-ESE 5-18.

GEOFON Data Centre, 1993. Geofon seismic network, Online data, Deutsches GeoForschungsZentrum GFZ, doi:10.14470/TR560404.

Gershenzon, N.I., Bambakidis, G. & Ternovskiy, I., 2014. Coseismic electromagnetic field due to the electrokinetic effect, *Geophysics,* **79**(5), E217–E229.

GFZ German Research Centre For Geosciences & Institut Des Sciences De L'Univers-Centre National De La Recherche CNRS-INSU, 2006. *IPOC seismic network,* Online data, Integrated Plate boundary Observatory Chile - IPOC, doi:10.14470/PK615318.

Grobbe, N. & Slob, E., 2016. Seismo-electromagnetic thin-bed responses: natural signal enhancements?, *J. geophys. Res.,* **121**(4), 2460–2479.

Haartsen, M.W. & Pride, S.R., 1997. Electroseismic waves from point sources in layered media, *J. geophys. Res.,* **102**(B11), 24 745–24 769.

Honkura, Y. *et al.*, 2000. Preliminary results of multidisciplinary observations before, during and after the Kocaeli (Izmit) earthquake in the western part of the North Anatolian Fault Zone, *Earth Planets Space,* **52**(4), 293–298.

Huang, Q., 2002. One possible generation mechanism of co-seismic electric signals, *Proc. Japan Acad. B,* **78**(7), 173–178.

Huang, Q., 2011. Retrospective investigation of geophysical data possibly associated with the M_S 8.0 Wenchuan earthquake in Sichuan, China, *J. Asian Earth Sci.,* **41**(4), 421–427.

Ivanov, A., 1939. Effect of electrization of earth layers by elastic waves passing through them, *Dokl. Akad. Nauk SSSR,* **24**(1), 42–45.

Jaafar, M., Vinogradov, J. & Jackson, M., 2009. Measurement of streaming potential coupling coefficient in sandstones saturated with high salinity NaCl brine, *Geophys. Res. Lett.,* **36**(21), doi:10.1029/2010JB007593.

Jardani, A. & Revil, A., 2015. Seismoelectric couplings in a poroelastic material containing two immiscible fluid phases, *Geophys. J. Int.,* **202**(2), 850–870.

Jardani, A., Revil, A., Slob, E. & Söllner, W., 2010. Stochastic joint inversion of 2D seismic and seismoelectric signals in linear poroelastic materials: a numerical investigation, *Geophysics,* **75**(1), N19–N31.

Jouniaux, L. & Zyserman, F., 2016. A review on electrokinetically induced seismo-electrics, electro-seismics, and seismo-magnetics for Earth sciences, *Solid Earth,* **7**(1), 249–284.

Konno, K. & Ohmachi, T., 1998. Ground-motion characteristics estimated from spectral ratio between horizontal and vertical components of microtremor, *Bull. seism. Soc. Am.,* **88**(1), 228–241.

Krischer, L., Megies, T., Barsch, R., Beyreuther, M., Lecocq, T., Caudron, C. & Wassermann, J., 2015. ObsPy: a bridge for seismology into the scientific Python ecosystem, *Comput. Sci. Discovery,* **8**(1), doi:10.1088/1749-4699/8/1/014003.

Lines, L. & Treitel, S., 1984. Tutorial: a review of least-squares inversion and its application to geophysical problems, *Geophys. Prospect.,* **32**(2), 159–186.

Matsushima, M. *et al.*, 2002. Seismoelectromagnetic effect associated with the Izmit earthquake and its aftershocks, *Bull. seism. Soc. Am.,* **92**(1), 350–360.

Matsushima, M., Honkura, Y., Kuriki, M. & Ogawa, Y., 2013. Circularly polarized electric fields associated with seismic waves generated by blasting, *Geophys. J. Int.,* **194**(1), 200–211.

Nagao, T., Orihara, Y., Yamaguchi, T., Takahashi, I., Hattori, K., Noda, Y., Sayanagi, K. & Uyeda, S., 2000. Co-seismic geoelectric potential changes observed in Japan, *Geophys. Res. Lett.,* **27**(10), 1535–1538.

Pride, S., 1994. Governing equations for the coupled electromagnetics and acoustics of porous media, *Phys. Rev. B,* **50**(21), doi:10.1103/PhysRevB.50.15678.

Downloaded from https://academic.oup.com/gji/article-abstract/217/1/108/5287972 by Bibliothek des Wissenschaftsparks Albert Einstein user on 08 March 2019

Pride, S.R. & Morgan, F., 1991. Electrokinetic dissipation induced by seismic waves, *Geophysics,* **56**(7), 914–925.

Rabbel, W., Iwanowski-Strahser, K., Strahser, M., Dzieran, L. & Thorwart, M., 2019. Seismoelectric field measurements in unconsolidated sediments in comparison with other methods of near-surface prospecting, in *The Seismoelectric Effect: Theory, Numerical Modeling, Laboratory and Field Experiments,* eds Grobbe, N., Revil, A., ,Zhu, Z. & Slob, E., Wiley Online Library, in press.

Ren, H., Huang, Q. & Chen, X., 2010. A new numerical technique for simulating the coupled seismic and electromagnetic waves in layered porous media, *Earthq. Sci.,* **23**(2), 167–176.

Ren, H., Wen, J., Huang, Q. & Chen, X., 2014. Electrokinetic effect combined with surface-charge assumption: a possible generation mechanism of coseismic EM signals, *Geophys. J. Int.,* **200**(2), 837–850.

Ren, H., Huang, Q. & Chen, X., 2015. Existence of evanescent electromagnetic waves resulting from seismoelectric conversion at a solid–porous interface, *Geophys. J. Int.,* **204**(1), 147–166.

Ren, H., Huang, Q. & Chen, X., 2018. Quantitative understanding on the amplitude decay characteristic of the evanescent electromagnetic waves generated by seismoelectric conversion, *Pure appl. Geophys.,* **175,** 2853–2879.

Revil, A. & Mahardika, H., 2013. Coupled hydromechanical and electromagnetic disturbances in unsaturated porous materials, *Water Resour. Res.,* **49**(2), 744–766.

Schakel, M., Smeulders, D., Slob, E. & Heller, H., 2011. Laboratory measurements and theoretical modeling of seismoelectric interface response and coseismic wave fields, *J. Appl. Phys.,* **109**(7), doi:10.1063/1.3567945.

Schurr, B. *et al.*, 2014. Gradual unlocking of plate boundary controlled initiation of the 2014 Iquique earthquake, *Nature,* **512**(7514), 299–302.

Sick, C. *et al.*, 2006. Seismic images of accretive and erosive subduction zones from the Chilean margin, in *The Andes,* pp. 147–169, eds Oncken, O., Chong, G., Franz, G., Giese, P., Götze, H.-J., Ramos, V.A., Strecker, M.R. & Wigger, P., Springer.

Strahser, M., Jouniaux, L., Sailhac, P., Matthey, P.-D. & Zillmer, M., 2011. Dependence of seismoelectric amplitudes on water content, *Geophys. J. Int.,* **187**(3), 1378–1392.

Thompson, A. & Gist, G., 1993. Geophysical applications of electrokinetic conversion, *Leading Edge,* **12**(12), 1169–1173.

Vargas, J.A., 2016. Large-scale distribution of fluids in the subduction zone of Northern Chile – constraints from magnetotelluric monitoring, *PhD thesis,* Freie Universität Berlin, Berlin, Germany.

Warden, S., Garambois, S., Jouniaux, L., Brito, D., Sailhac, P. & Bordes, C., 2013. Seismoelectric wave propagation numerical modelling in partially saturated materials, *Geophys. J. Int.,* **194**(3), 1498–1513.

Wessel, P., Smith, W.H., Scharroo, R., Luis, J. & Wobbe, F., 2013. Generic mapping tools: improved version released, *Eos, Trans. Am. geophys. Un.,* **94**(45), 409–410.

Zyserman, F., Monachesi, L. & Jouniaux, L., 2016. Dependence of shear wave seismoelectrics on soil textures: a numerical study in the vadose zone, *Geophys. J. Int.,* **208**(2), 918–935.

APPENDIX A: HALF-SPACE MODEL SPECIFICATIONS

In this section, we provide the computational settings used to calculate the spectra and snapshots illustrated in Section 2, Fig. 2.

For the calculations we used the code provided by Garambois & Dietrich (2002), that is described in Section 4.1. The subsurface model consists of two layers. The upper and lower layers have the properties of layers 1 and 2, respectively that are described in Tables 3 and B1. The source is a vertical point force that is located 5 km beneath the layers' interface.

The spectra shown in Figs 2(a) and (b) were calculated for a receiver at 50-km epicentral distance from the source. The receiver was placed at a free surface 100 m above the interface. Only the fast *P* wave, coseismic field and IRs were considered in the calculation. The seismic and SE spectra were calculated for a timelength of 204.8 s over 4096 samples, resulting in a sampling rate of 20 Hz. The spectra were then smoothed with the Konno–Ohmachi smoothing filter and divided to calculate the SESRs in Fig. 2(c).

The snapshots shown in Figs 2(d) and (e) were calculated for a timelength of 40.96 s over 2048 samples, resulting in a sampling rate of 50 Hz. 101 receivers were evenly distributed in the horizontal direction between 40- and 60-km offset, resulting in a spacing of 200 m. In the vertical direction, 51 receivers were placed between 0 km (source depth) and 10 km, resulting also in a spacing of 200 m. For clarity, the free surface reflections were omitted. A source wavelet in the form of

$$w(t) = \sin\left(\pi \frac{t}{T_0}\right) - \frac{1}{3}\sin\left(3\pi \frac{t}{T_0}\right) \tag{A1}$$

was applied to the data in the time domain, with $T_0 = 1$ s. The results presented in Figs 2(d) and (e) correspond to the time of 20 s after nucleation.

APPENDIX B: MODEL PARAMETERS

Table B1 lists the input parameters used to calculate the modelled SESRs. Parameters marked with (∗) were calculated by the program. The corresponding equations can be found in Garambois & Dietrich (2002) and Warden *et al.* (2013).

The modelling code is mainly intended for near surface applications. To be able to model the resistivities suggested by Vargas (2016), high salinity values had to be chosen for greater depths. Using the zeta-potential formula $\zeta = 0.008 \cdot 0.026 \cdot \log_{10}(\text{salinity})$ of Pride & Morgan (1991), that is implemented in the modelling code, leads to an unrealistically high-zeta-potential value. Jaafar *et al.* (2009) suggested that for high salinities (above 0.2 mol l^{-1}) the zeta potential remains constant at around −0.02 V. We therefore used this value for the zeta potential of layers 4–8.

Downloaded from https://academic.oup.com/gji/article-abstract/217/1/108/5287972 by Bibliothek des Wissenschaftsparks Albert Einstein user on 08 March 2019

Table B1. Input parameters to calculate SESRs in Section 4.1. Parameters marked with (∗) were computed by the program. The **bold parameters** were changed to adjust the modelled SESR to the measured SESR and altered in the inversion.

Layer	1	2	3	4	5	6	7	8
Depth (km)	**0.1**	**0.3**	**2.5**	7	22	37	50	500
Porosity (per cent)	**20**	**5**	**1**	0.5	0.1	0.1	0.1	0.1
Saturation (-)	0.75	1.0	1.0	1.0	1.0	1.0	1.0	1.0
Permeability (Darcy)	**0.1**	**0.1**	**0.1**	0.01	0.01	0.01	0.01	0.01
Solid bulk modulus (GPa)	8.2	8.2	15.9	54.7	63.0	72.8	78.1	116.0
Solid shear modulus (GPa)	5.9	5.9	9.8	33.1	37.9	43.8	46.9	69.7
Fluid bulk modulus (GPa)	2.27	2.27	2.27	2.27	2.27	2.27	2.27	2.27
Air bulk modulus (kPa)	100	100	100	100	100	100	100	100
Consolidation parameter (-)	5	2	2	2	2	2	2	2
Fluid viscosity (Pa s)	0.001	0.001	0.001	0.001	0.001	0.001	0.001	0.001
Air viscosity (Pa s)	1.80E-05	1.8E-05	1.8E-05	1.8E-05	1.8E-05	1.8E-05	1.8E-05	1.8E-05
Solid density (kg m^{-3})	2194	2194	2312	2710	2767	2831	2864	3256
Fluid density (kg m^{-3})	1000	1000	1000	1000	1000	1000	1000	1000
Air density (kg m^{-3})	1	1	1	1	1	1	1	1
Salinity (mol l^{-1})	**0.0095**	**0.014**	**0.013**	0.3	1.0	1.0	1.0	1.0
Temperature (K)	300	300	300	320	450	450	600	1000
Fluid permittivity (-)	80	80	80	80	80	80	80	80
Solid permittivity (-)	4	4	4	4	4	4	4	4
Cementation exponent (-)	1.3	1.3	1.3	1.5	1.5	1.5	1.5	1.5
$*v_P$ (km s^{-1})	1.87	2.57	3.5	6.0	6.4	6.8	7.0	8.0
$*v_S$ (km s^{-1})	1.00	1.51	2.02	3.47	3.69	3.93	4.04	4.62
$*v_{EM}$ at 2 Hz (km s^{-1})	25.8	43.5	128.7	71.4	130.8	130.8	130.8	130.8
∗Density (kg m^{-3})	1905	2134	2299	2701	2765	2829	2862	3254
∗Zeta potential (V)	−0.045	−0.04	−0.041	−0.02	−0.02	−0.02	−0.02	−0.02
∗Fluid conductivity (S m^{-1})	0.088	0.13	0.12	2.78	9.28	9.28	9.28	9.28
∗Bulk resistivity (Ωm)	134	378	3302	1016	3409	3409	3409	3409

Downloaded from https://academic.oup.com/gji/article-abstract/217/1/108/5287972 by Bibliothek des Wissenschaftsparks Albert Einstein user on 08 March 2019